Geometry induced sequence of nanoscale Frank–Kasper and quasicrystal mesophases in giant surfactants

Kan Yue[a,1], Mingjun Huang[a,1], Ryan L. Marson[b,1], Jinlin He[c], Jiahao Huang[a], Zhe Zhou[a], Jing Wang[a], Chang Liu[a], Xuesheng Yan[c], Kan Wu[a], Zaihong Guo[d], Hao Liu[a], Wei Zhang[a], Peihong Ni[c], Chrys Wesdemiotis[a,d], Wen-Bin Zhang[e,2], Sharon C. Glotzer[b,f,2], and Stephen Z. D. Cheng[a,2]

[a]Department of Polymer Science, College of Polymer Science and Polymer Engineering, The University of Akron, Akron, OH 44325-3909; [b]Department of Materials Science and Engineering, University of Michigan, Ann Arbor, MI 48109; [c]College of Chemistry, Chemical Engineering and Materials Science, Soochow University, Suzhou 215123, China; [d]Department of Chemistry, The University of Akron, Akron, OH 44325; [e]Key Laboratory of Polymer Chemistry & Physics of Ministry of Education, Centre for Soft Matter Science and Engineering, College of Chemistry and Molecular Engineering, Peking University, Beijing 100871, China; and [f]Department of Chemical Engineering, University of Michigan, Ann Arbor, MI 48109

Edited by Frank S. Bates, University of Minnesota, Minneapolis, and accepted by Editorial Board Member David A. Tirrell November 2, 2016 (received for review June 10, 2016)

Frank–Kasper (F-K) and quasicrystal phases were originally identified in metal alloys and only sporadically reported in soft materials. These unconventional sphere-packing schemes open up possibilities to design materials with different properties. The challenge in soft materials is how to correlate complex phases built from spheres with the tunable parameters of chemical composition and molecular architecture. Here, we report a complete sequence of various highly ordered mesophases by the self-assembly of specifically designed and synthesized giant surfactants, which are conjugates of hydrophilic polyhedral oligomeric silsesquioxane cages tethered with hydrophobic polystyrene tails. We show that the occurrence of these mesophases results from nanophase separation between the heads and tails and thus is critically dependent on molecular geometry. Variations in molecular geometry achieved by changing the number of tails from one to four not only shift compositional phase boundaries but also stabilize F-K and quasicrystal phases in regions where simple phases of spheroidal micelles are typically observed. These complex self-assembled nanostructures have been identified by combining X-ray scattering techniques and real-space electron microscopy images. Brownian dynamics simulations based on a simplified molecular model confirm the architecture-induced sequence of phases. Our results demonstrate the critical role of molecular architecture in dictating the formation of supramolecular crystals with "soft" spheroidal motifs and provide guidelines to the design of unconventional self-assembled nanostructures.

self-assembly | Frank–Kasper phases | quasicrystal phases | giant surfactants | POSS

In addition to the close-packing schemes of identical atoms (such as hexagonal close-packing and face-centered cubic), atoms with different radii and electronic states in metal alloys are able to pack into more complex phases composed of spheres, such as the Frank–Kasper (F-K) phases (1, 2), which combine the Frank lattice (icosahedron with a coordination number of 12) and the Kasper lattice (with higher coordination numbers of 14, 15, and 16). A few F-K phases such as the A15- (space group of $Pm\bar{3}n$) and σ- (space group of $P4_2/mnm$) phases are periodic approximants of different quasicrystals. Quasicrystals, first identified in supercooled metal alloys, are aperiodic, and possess 5-, 7-, 8-, 10-, or 12-fold rotational symmetry but no long-range translational periodicity (3–5). Stabilization of these phases in metals originates from both geometric factors and the tendency to enhance low orbital electron sharing due to fewer surface contacts among the atoms (6).

F-K phases have also been identified in soft-matter systems, including small-molecule surfactants (7–9), block copolymers (10–12), dendrimers (13–15), liquid crystals (16, 17), colloidal particles (18), and, very recently, molecular giant tetrahedra (19). In contrast to metal alloys that use atoms as the motifs, organic/hybrid molecules first self-assemble into spheroidal motifs (micelles), and the motifs further organize into supramolecular lattices. Dodecagonal quasicrystals (DQCs) with 12-fold rotational symmetry have also been reported; representative examples include mesoporous silica constructed from small-molecule surfactant micelles (20), micelles of linear diblock copolymers (21), specifically designed single-component dendrimers (22), and tetrablock copolymers (23). Very recently, a DQC phase was identified as a metastable state in supercooled diblock copolymer melts (24).

Despite these successes, observations of these unconventional ordered phases of spheroids in soft materials largely rely on serendipity. A grand challenge is to understand the structural evolution pathways and relationships among these different phases, and to control the spatial packing of the supramolecular spheroidal motifs into targeted nanostructures (25). Self-assembling polymeric materials (such as block copolymers) offer almost unlimited freedom to tailor the chemical structures of the materials and control the size and packing symmetry of the phase-separated

Significance

How far can we push self-assembly toward unusual nanostructures? Frank–Kasper and quasicrystal phases represent unconventional phases of ordered spheroids originally identified in metal alloys. We report that Frank–Kasper and quasicrystal phases and their transition sequence are observed in one-component giant surfactants by introducing variations in molecular geometry. Both X-ray scattering and electron microscopy techniques are used to identify the self-assembled nanostructures. Combining molecular dynamics simulations, we attribute the appearance of these phases to molecular geometry as a result of tail number variation. Our findings lay the foundation for rational design of unconventional soft-matter phases and for exploiting them for unusual properties and functions.

Author contributions: K.Y., M.H., R.L.M., W.-B.Z., S.C.G., and S.Z.D.C. designed research; K.Y., M.H., R.L.M., J. He, J. Huang, Z.Z., J.W., C.L., X.Y., K.W., Z.G., H.L., W.Z., P.N., and C.W. performed research; K.Y., M.H., R.L.M., J. He, J. Huang, Z.Z., J.W., C.L., X.Y., K.W., Z.G., H.L., W.Z., P.N., and C.W. contributed new reagents/analytic tools; K.Y., M.H., R.L.M., J. He, W.-B.Z., S.C.G., and S.Z.D.C. analyzed data; and K.Y., M.H., R.L.M., W.-B.Z., S.C.G., and S.Z.D.C. wrote the paper.

The authors declare no conflict of interest.

This article is a PNAS Direct Submission. F.S.B. is a Guest Editor invited by the Editorial Board.

[1]K.Y., M.H., and R.L.M. contributed equally to this work.

[2]To whom correspondence may be addressed. Email: wenbin@pku.edu.cn, sglotzer@umich.edu, or scheng@uakron.edu.

This article contains supporting information online at www.pnas.org/lookup/suppl/doi:10.1073/pnas.1609422113/-/DCSupplemental.

nanodomains. Notably, the geometric effect on phase diagrams of diblock copolymers has been theoretically assessed (26, 27). It is argued that besides the commonly observed body-centered cubic (BCC) phase in linear diblock copolymers, the A15- and σ-phases should be stable in linear-branched diblock copolymers with large conformational asymmetry (26, 27).

Here, we present an experimental study on the self-assembly of a series of four giant surfactants based on polyhedral oligomeric silsesquioxane (POSS). These giant surfactants are designed to possess different molecular geometries by attaching $n = 1$–4 identical polystyrene (PS) tails onto a single vertex of a hydrophilic POSS cage (DPOSS-nPS$_m$, Fig. 1). Nanophase separation between the hydrophilic POSS cages and the hydrophobic PS tails drives the formation of various highly ordered nanostructures in the bulk with feature sizes around 10 nm. When $n = 1$ or 2, the phase transitions display the conventional sequence as found in typical diblock copolymers, such as the usual BCC micellar phase, hexagonal cylindrical phase (HEX), and lamellar phase (LAM), but with shifted phase boundaries in terms of volume fraction of the PS tails (v_f^{PS}) as previously predicted (28, 29). More importantly, when $n = 3$ or 4, stable A15-, σ-, and DQC phases are identified in the spheroidal micelle region of the phase diagram, resulting in a distinct sequence of transitions from one phase to the next with increasing v_f^{PS}.

Results and Discussion

Giant surfactants DPOSS-nPS$_m$ are synthesized following the sequential "click" chemistry approach (30–32) with precisely defined chemical compositions, molecular geometry, and narrow polydispersity (*SI Appendix*, Figs. S1–S17). Fourteen hydroxyl groups cap the seven nontethered vertices of the POSS cages to provide sufficient immiscibility and driving force for phase separation. These samples reflect a systematic, two-parameter control in primary chemical structures. Within each series, the POSS head group is fixed and the lengths of the PS tails are varied to tune v_f^{PS} of each sample. Among the different series, variation in n leads to variations in molecular geometry (Fig. 1). Thermal annealing processes are applied to generate self-assembled nanostructures of the DPOSS-nPS$_m$ samples, which are studied via combined techniques of small-angle X-ray scattering (SAXS) (in reciprocal space) on the bulk samples and bright-field (BF) transmission electron microscopy (TEM) (in real space) on microtomed sample sections.

The phase transition sequence of the DPOSS-1PS$_m$ giant surfactants recently has been reported to be similar to that of flexible diblock copolymers (33). With increasing length of the PS tails, the phase structure sequence follows LAM → double gyroids (DGs, space group $Ia\bar{3}d$) → HEX → BCC (space group $Im3m$) spheroidal micelles. To obtain more complex supramolecular structures, we start from the DPOSS-4PS$_m$ samples with the most distinct geometrical variation. The DPOSS-4PS$_6$ sample with the shortest PS tail length shows an HEX phase at $v_f^{PS} = 0.75$, based on the SAXS pattern with scattering vector q ratios of $1{:}\sqrt{3}{:}\sqrt{4}$ (Fig. 2*A*). This assignment is confirmed by the BF TEM image (Fig. 2*F*) showing an HEX packing of columns, as revealed by the fast Fourier transformation (FFT) diffraction pattern (Fig. 2*F*, *Inset*).

All of the other DPOSS-4PS$_m$ samples with longer tails than PS$_6$ fall into the spheroidal micelle phase region, and show the A15-, σ-, and DQC phases before reaching the BCC phase. Specifically, DPOSS-4PS$_{10}$ ($v_f^{PS} = 0.82$) shows q ratios of $\sqrt{2}{:}\sqrt{4}{:}\sqrt{5}{:}\sqrt{6}{:}\sqrt{8}{:}\sqrt{10}{:}\sqrt{17}{:}\sqrt{21}$ in its SAXS pattern (Fig. 2*B*), suggesting the formation of a highly ordered A15 phase with a cubic unit cell (a = 13.1 nm). A BF TEM image (Fig. 2*G*) confirms the characteristic square 4^4 tiling and FFT diffraction pattern, in accordance with the A15 structure along the [001] zone as shown in Fig. 2*K* (19). For DPOSS-4PS$_{13}$ ($v_f^{PS} = 0.86$), a different SAXS pattern (Fig. 2*C*) with multiple sharp diffraction peaks was recorded, which perfectly matches the pattern of a σ-phase with a tetragonal unit cell (a = 25.7 nm, c = 13.4 nm) (10). These well-resolved diffraction peaks can be clearly indexed (*SI Appendix*, Fig. S18 and Table S1). The corresponding BF TEM image along the [001] direction (Fig. 2*H*) displays a typical $3^2.4.3.4$ tiling number (Fig. 2*L*), and the FFT diffraction pattern (Fig. 2*H*, *Inset*) sharply reveals the tetragonal lattice of the σ-phase (10).

For DPOSS-4PS$_{15}$ ($v_f^{PS} = 0.87$), a DQC phase is identified based on combined SAXS (Fig. 2*D*) and BF TEM (Fig. 2*I*) results. The SAXS pattern has nearly the identical features and q-value ratios of the reported DQC phase in a dendrimer system (22) and diblock copolymer melts (24), which can be indexed using a 5D reciprocal lattice (*SI Appendix*, Fig. S19 and Table S2). In particular, the 12 strong diffraction spots in the FFT pattern reveal

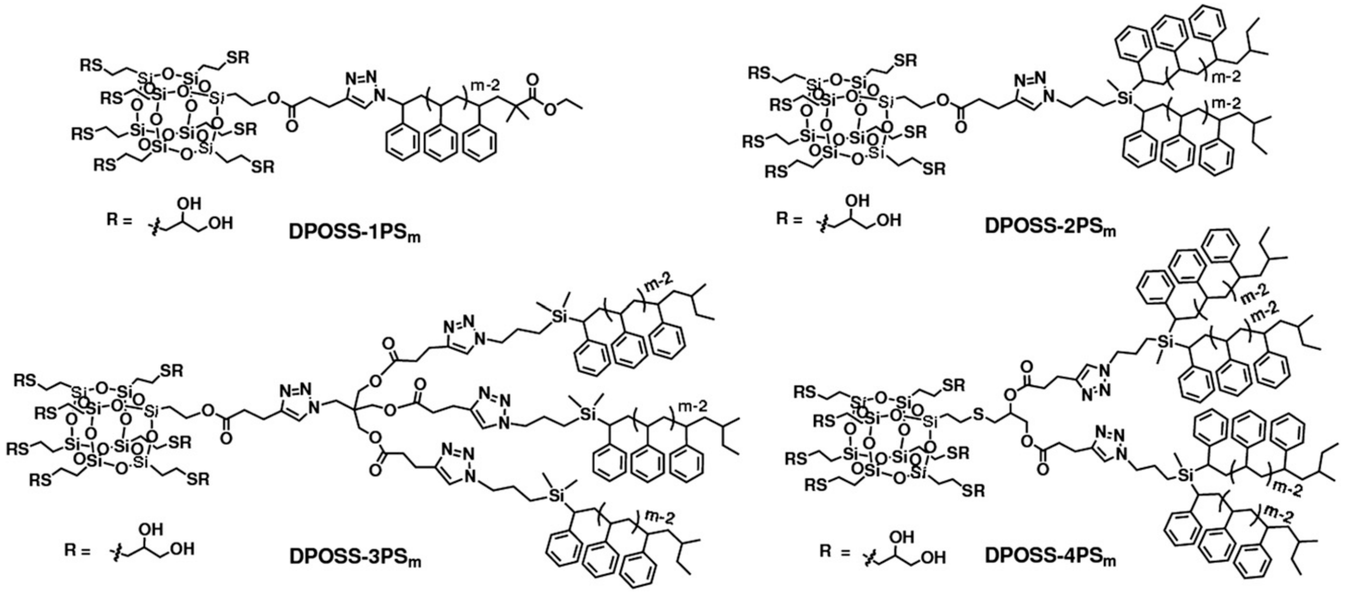

Fig. 1. Chemical structures of the DPOSS-nPS$_m$ giant surfactants with geometrical variations. n indicates the number of tails (tethers) emanating from a single vertex in each molecule; m is the statistical degree of polymerization of each PS tail.

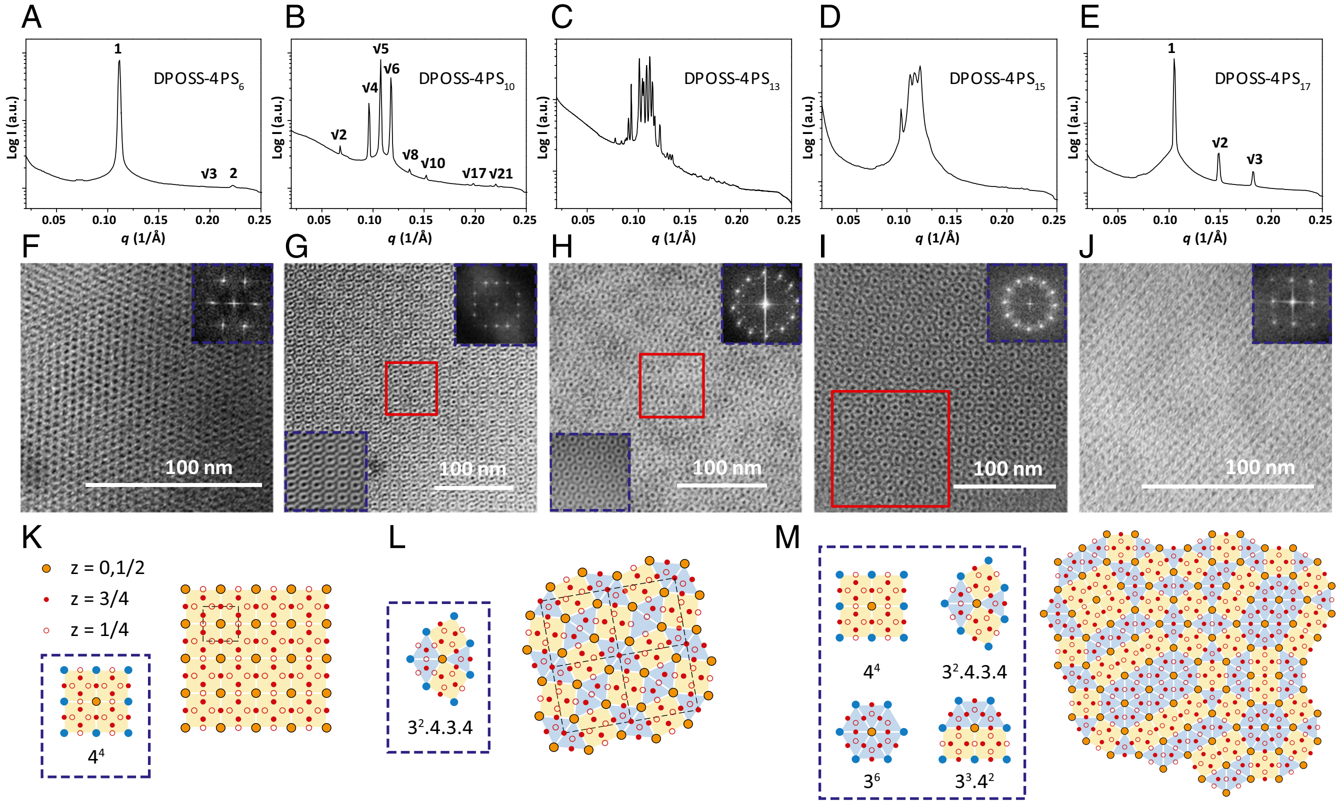

Fig. 2. Self-assembly phase structures of DPOSS-4PS$_m$ giant surfactants. SAXS patterns and BF TEM images of five representative DPOSS-4PS$_m$ samples showing the HEX phase in *A* and *F*, the A15 phase in *B* and *G*, the σ-phase in *C* and *H*, the DQC phase in *D* and *I*, and the BCC phase in *E* and *J*. TEM images are taken along the [001] direction of the HEX phase in *F*, the [001] direction of the A15 phase in *G*, the [001] direction of the σ-phase in *H*, the [00001] direction of the DQC phase in *I*, and the [001] direction of the BCC phase in *J*. The upper right insets of the TEM images are corresponding FFT patterns and the bottom left insets in *G* and *H* show the local TEM image after Fourier filtering. Two-dimensional tiling patterns of (*K*) the A15 phase, (*L*) the σ-phase, and (*M*) the DQC phase are abstracted from the TEM images bounded by the red-line boxes shown in *G*–*I*, respectively. The observed basic elements and tiling numbers are summarized in the boxes.

the 12-fold rotational symmetry within the layer (Fig. 2*I*, *Inset*). From the BF TEM image along the [00001] direction (Fig. 2*I*), representative tiling numbers of $3^2.4.3.4$, $3^3.4^2$, 4^4, and 3^6 can all be identified (Fig. 2*M*), further supporting the formation of an aperiodic DQC phase with ordered layered structures along the [00001] direction (22, 24). A detailed analysis of the BF TEM image showing a random-tiling DQC is presented in *SI Appendix*, Fig. S20. Finally, in DPOSS-4PS$_{17}$ ($v_f^{PS} = 0.88$), a BCC phase appears, as indicated by the q ratio of $1{:}\sqrt{2}{:}\sqrt{3}$ in the SAXS pattern (Fig. 2*E*) and the BF TEM image with the FFT diffraction pattern (a = 8.46 nm, Fig. 2*J*, *Inset*). The phase structure assignments and parameters are summarized in *SI Appendix*, Table S3.

To further elucidate the effects of molecular geometry, we further investigate DPOSS-3PS$_m$ and DPOSS-2PS$_m$ samples. Combining the SAXS and BF TEM results, it is evident that the DPOSS-3PS$_m$ samples show similar phase transition behavior to that of the DPOSS-4PS$_m$ series, with an observed sequence of A15 → σ → DQC → BCC with increasing v_f^{PS} (*SI Appendix*, Figs. S21 and S22 and Tables S4 and S5). We did not observe the HEX phase in the DPOSS-3PS$_m$ series because PS tails with low enough molecular weights were not available. On the other hand, the observed phase transition sequence of the DPOSS-2PS$_m$ samples is identical to that of the DPOSS-1PS$_m$ series, following a sequence of LAM → DG → HEX → BCC (*SI Appendix*, Fig. S23). More details on phase identification of these four series of samples are in the *SI Appendix*. Furthermore, in temperature-resolved SAXS experiments, no order–disorder or order–order phase transitions were recorded for the F-K and DQC phases up to the corresponding decomposition temperatures (*SI Appendix*, Fig. S24). This suggests the stability of these complex phases, which either are thermodynamically stable or kinetically trapped, long-lived metastable phases (24).

We construct a phase boundary diagram to summarize the structures and transition sequences as shown in Fig. 3. It is evident that the phase boundaries of the conventional phases (LAM, DG, HEX, and spheroidal micelle phases) shift to lower v_f^{PS} values with increasing number of PS tails. This is because the presence of multiple tails at the junction point creates shape asymmetry at the interfaces, and contributes to the interfacial curvature between immiscible nanodomains in addition to changing v_f^{PS}. Theoretical studies on polymer-tethered POSS conjugates with different architectures (28, 29) and on linear-branched diblock copolymers (26, 27) predict similar results. The phase diagrams of DPOSS-3PS$_m$ and DPOSS-4PS$_m$ include F-K and quasicrystal phases in the spheroidal micelle region of the phase diagram, resulting from the molecular geometric changes (Fig. 3).

Although the formation mechanisms of these F-K and DQC phases have been investigated previously (34, 35), those tested model systems possessed significant variations in terms of chemical structures and interactions. Therefore, we perform Brownian molecular dynamics (BD) simulations to confirm that the observed rich phase behaviors are dictated primarily by molecular geometry, rather than chemistry, which can suggest insights to elucidate the assembly mechanism. Detailed modeling of the hydrogen bonding interactions and rigid conformations of the DPOSS cages is computationally challenging, and would limit accessible time scales, even on large computers, to times well below that needed to observe self-assembled phases. Instead, our coarse-grained model

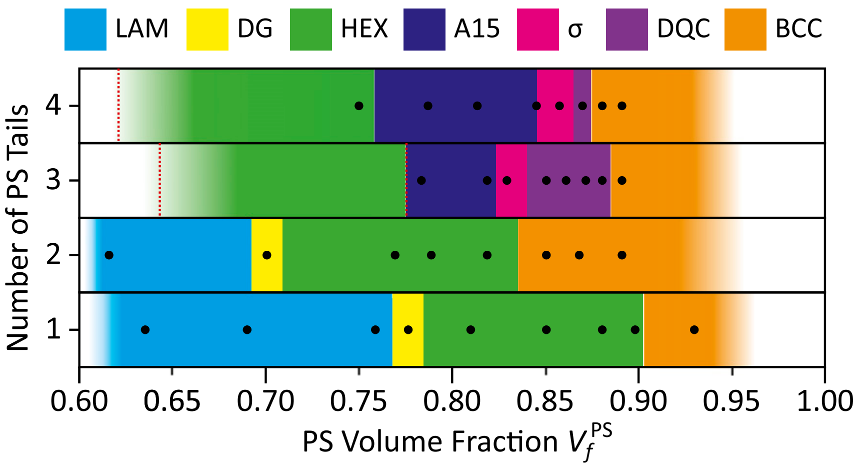

Fig. 3. Experimental phase boundary diagrams of DPOSS-nPS$_m$ (n = 1–4) giant surfactants with different molecular geometry. Regions for different phases are shown in different colors as indicated by the legends. Experimental observations of the LAM phase in DPOSS-3PS$_m$ and DPOSS-4PS$_m$, and of the HEX phase in DPOSS-3PS$_m$, are limited by the unavailability of PS tails with low enough molecular weights. The F-K and DQC phases are only observed in DPOSS-3PS$_m$ and DPOSS-4PS$_m$. The black dots represent experimentally accessed data points. The dashed lines are speculated phase boundaries for illustration purposes only.

serves as a qualitative yet valuable approach to evaluate the molecular geometric effects in the giant surfactant system. Although we do not expect to predict, with quantitative accuracy, volume fractions of specific phase, average micelle sizes, etc., we do expect our model to predict the experimentally observed phases and their relationship to molecular architecture.

The model and simulation method are adapted from our previous studies of tethered nanoparticles (29, 34, 36); full details on the potentials used, and thermodynamic parameters, are available in *SI Appendix*, section 2.4. The DPOSS heads are modeled as cubes by bonding overlapping spheres with stiff harmonic springs. To capture immiscibility between the solvent and DPOSS molecules, like species attract via a Lennard-Jones (LJ) potential; cross-interactions between cube and polymer beads are strictly repulsive via a Weeks–Chandler–Anderson potential, which is a shifted and truncated version of the LJ potential. The volume ratio between a DPOSS cage and a styrene monomer is matched to the experimental volumes calculated from density measurements. Degree of polymerization of the PS tails attached to a single vertex of the DPOSS cages is tuned by the number of coarse-grained polymer beads per tail, which ranges from m = 5 to 14. An example model of DPOSS-4PS$_7$ is shown in Fig. 4*A*.

To perform the simulation, 2,000 DPOSS-4PS$_m$ molecules are placed in a cubic box with periodic boundary conditions. BD simulations are run at 20 volume fractions between $\phi = 0.40$ and 0.50, where ϕ is the volume fraction of the overall molecules with respect to the overall volume of the simulation box. Simulations are thermalized to randomize the positions and conformations of

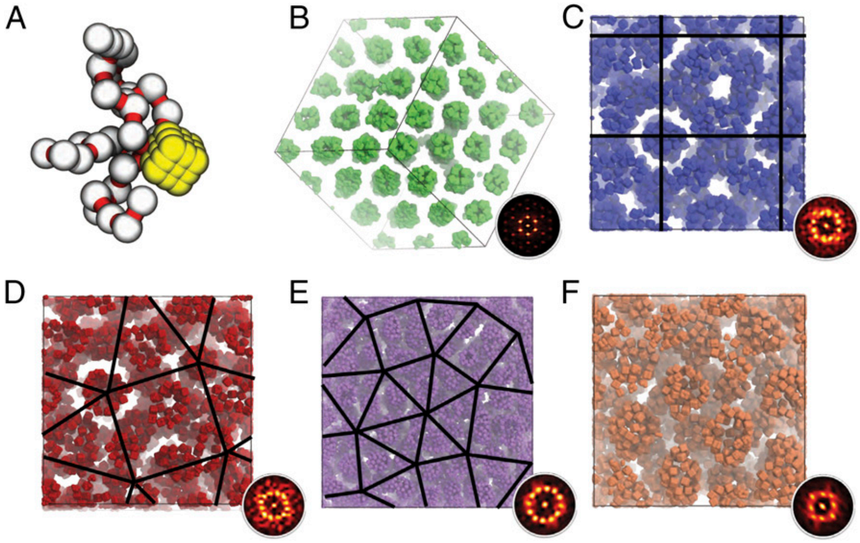

Fig. 4. Molecular dynamics simulation results of DPOSS-4PS$_m$. (*A*) Simulation model of an individual DPOSS-4PS$_7$ molecule. The DPOSS cage (shown in yellow) is constructed from 26 bonded beads; the beads representing PS monomers are shown in white connected by red bonds. In all cases hydrophilic POSS heads form the core of independent aggregates (columns or spheres). (*B*) View of HEX phase along the [001] direction from m = 4, ϕ = 0.50. (*C*) F-K regions containing mixed A15 and σ-phases at m = 7, ϕ = 0.41 (here the A15 lattice is shown). (*D*) σ-Region with characteristic 3^2.4.3.4 tiling at m = 8, ϕ = 0.45. (*E*) View from the *z* axis of a DQC-like structure at m = 9, ϕ = 0.43, and an aspect ratio of 1.28:1.28:1, along with characteristic 12-fold diffraction pattern. Periodic layered structures are observed along the *z* axis. (*F*) View of a BCC phase along the [001] direction at m = 10, ϕ = 0.43. (*Insets*) Corresponding FFT patterns of the 3D images, which are taken from the center-of-mass positions of the cubic head-groups.

the molecules, slowly compressed to the operating volume fraction, and then run for sufficient time steps to achieve equilibration, as determined by monitoring, e.g., the system energy and average cluster size (see *SI Appendix*, section 2.4 for details). Over the course of the simulation, DPOSS-4PS$_m$ aggregate to form either cylindrical or spheroidal motifs, which then further order to form supramolecular lattices. Molecules exchange between clusters, and equilibrate to an average number of molecules per micelle (*SI Appendix*, Fig. S25).

By varying the length of the polymer tails, the simulations produce a sequence of phase transitions identical to that observed in our experiments. At the shortest tether lengths of m = 4, the HEX phase forms (Fig. 4*B*). For intermediate tail lengths (m = 7–9), we observe a region of ordered supramolecular lattices with features of the A15-, σ-, and DQC phases (Fig. 4 *C*–*F*), respectively. Finally, at the longest tether lengths we observe the formation of a BCC supramolecular lattice (Fig. 4*G*). We note that due to the aperiodic nature of the DQC phase, larger simulations of 15,000 DPOSS in noncubic boxes of varying aspect ratios are used to obtain structures that exhibit (pseudo)–12-fold symmetry with periodic ordered layers along the 12-fold symmetry axis of the experimentally observed DQC phase.

What is the origin of these complex phases in multitailed giant surfactants? Hydrophilic DPOSS heads aggregate via collective hydrogen bonding interactions to form the micelle cores, which are surrounded by PS shells. In phase-separated ordered structures, there is an interfacial tension between the PS and DPOSS domains, which results from chemical incompatibility between the DPOSS cages and PS tails and is proportional to both the χ-interaction parameter and the overall interfacial area between the immiscible domains. According to previous theoretical predictions on linear-branched block copolymers (26), the balance between the interfacial tension and the stretching entropy of the PS tails, which increases with increasing tail length, determines how the molecules organize within the micelles. When the micelles are further assembled into ordered phases, it is known that compared with the BCC phase, the A15- and σ-phases have smaller overall contacting areas among neighboring micelles (10, 11, 35). Therefore, based on the assumption of constant χ-parameter, the micelles in the A15- and σ-phases possess relatively low interfacial tension, which is achieved at the penalty of relatively high stretching energies compared with those in the BCC phase.

In addition, in the F-K and DQC spheroidal micelle phases, the assembled micelles do not necessarily have a uniform size distribution, as experimentally proven by our recent study (19). As previously predicted (34), even a small size (or shape) polydispersity is sufficient to disrupt the local close packing of FCC and BCC phases and instead favor F-K phases, especially in brushy micelles. Indeed, we observe a roughly bimodal distribution of micelle sizes in the A15 phase in our simulations of DPOSS-4PS$_m$ (*SI Appendix*, Fig. S26*A*). Regrettably, upon closer examination of the TEM image of the A15 phase formed by DPOSS-4PS$_{10}$ using Fourier filtering treatment and color reversion as reported in our previous study (19), it is difficult to quantify this size distribution experimentally (*SI Appendix*, Fig. S27). In contrast to the A15 phase, a unimodal distribution of micelle sizes is observed in the simulated BCC phase (*SI Appendix*, Fig. S26*B*). Considering the more complex nature of other F-K phases and the DQC phase, identification of size distribution of spheres in these unconventional phases remains a grand challenge. Once formed, the observed phases are further stabilized by a reduction in free energy achieved by deformation of the flexible micelle shells into polyhedra that adopt the shape of the Voronoi cells associated with that particular crystal (11, 35). Furthermore, the multitailed architecture of DPOSS-3PS$_m$ and DPOSS-4PS$_m$ expands the spheroidal micelle phase to lower values of v_f^{PS}, where the reduced entropic penalty from stretching of relatively short PS tails facilitates the formation of the F-K and DQC phases.

This explanation agrees with that given in our previous study on the relative entropic stability of the A15-, DQC-, and BCC phases, and the role of micellar shape polydispersity (34). Observations of stable A15- and σ-phases indicate that in their own v_f^{PS} regions, the stretching energy penalty is relatively low due to the short PS tails. As the PS tails become longer, the BCC phase, which facilitates maximizing conformational entropy (minimizing the stretching energy), becomes stable. Specifically, existence of the DQC phase between the σ- and BCC phases must originate in a disordering process of the σ-phase to form a range of polyhedral sizes to provide the combined tiling numbers before entering the ordered BCC phase. The geometric effect observed in giant surfactants provides a guide to fine control intra- and intermicellar interactions toward the stabilization of unusual packing schemes of supramolecular spherical motifs in other soft-matter systems.

Methods

Synthesis. Giant surfactants were synthesized following the developed sequential click reactions with modifications, as described in refs. 30–32. More details on the molecular design and synthesis are provided in *SI Appendix*, section 1.

Characterization. SAXS experiments were performed on a Rigaku MicroMax 002+ instrument equipped with a 2D multiwire area detector and a microfocus sealed copper tube. BF TEM images of the thin-slice samples were recorded on a JEOL-1230 TEM with an accelerating voltage of 120 kV on a digital CCD camera. More details on the characterization are provided in *SI Appendix*, section 1.

Fourier Filtering. Fourier filtering of the TEM image was carried out following the method reported in ref. 19. More details on the Fourier filtering are provided in *SI Appendix*, section 1.

Sample Preparation. Samples with self-assembled nanostructures for SAXS experiments were prepared by putting the vacuum-dried samples into an aluminum sample holder (15 mm × 10 mm × 1 mm) with a hole (5 mm in diameter) in the center. The sample holders were sealed with Kapton tapes, heated to 150 °C under nitrogen atmosphere, and annealed at that temperature for 30 min to several hours. Development of the ordered structures was monitored by SAXS measurements. Thin slices of the annealed samples were obtained from unoriented samples that embedded in epoxy monolith at room temperature by using a Leica EM UC7 Ultracryomicrotome equipped with a Diatome Cryo diamond knife. Thin slices were subsequently transferred to copper grids coated with amorphous carbon for TEM experiments. Typical thickness of the slices was 70–100 nm. In most cases, staining is not necessary for the microtomed samples due to the strong electron density contrast between DPOSS cages and PS chains. Whenever necessary, staining of the thin slice samples was performed by using OsO_4 for the DPOSS cages at room temperature for 12 h.

ACKNOWLEDGMENTS. R.L.M. is grateful to M. Eric Irrgang, Matthew Spellings, and Joshua Anderson for fruitful discussions. Supported by National Science Foundation (NSF) Grant DMR-1408872 (to S.Z.D.C.), US Army Research Office Grant W911NF-10-1-0518 (to S.C.G.), National Natural Science Foundation of China 21304061 (to J.H. and P.N.), Natural Science Foundation of Jiangsu Province BK20130286 (to J.H. and P.N.), and NSF Grant CHE-1308307 (to C.W.). Use of the Advanced Photon Source at Argonne National Laboratory was supported by the US Department of Energy (DOE), Office of Science, and Office of Basic Energy Sciences. Simulations were run on the resources of the Oak Ridge Leadership Computing Facility, which is a DOE Office of Science User Facility supported under Contract DE-AC05-00OR22725.

---

1. Frank FC, Kasper JS (1959) Complex alloy structures regarded as sphere packings. II. Analysis and classification of representative structures. *Acta Crystallogr* 12:483–499.
2. Frank FC, Kasper JS (1958) Complex alloy structures regarded as sphere packings. I. Definitions and basic principles. *Acta Crystallogr* 11:184–190.
3. Levine D, Steinhardt PJ (1984) Quasicrystals: A new class of ordered structures. *Phys Rev Lett* 53(26):2477–2480.
4. Shechtman D, Blech I, Gratias D, Cahn JW (1984) Metallic phase with long-range orientational order and no translational symmetry. *Phys Rev Lett* 53(20):1951–1953.

5. Gähler F (1988) *Quasicrystalline Materials* (World Scientific, Singapore), pp 272–284.
6. Graef MD, McHenry ME (2012) *Structure of Materials: An Introduction to Crystallography, Diffraction and Symmetry* (Cambridge Univ Press, Cambridge, UK), 2nd Ed, pp 466–496.
7. Vargas R, Mariani P, Gulik A, Luzzati V (1992) Cubic phases of lipid-containing systems. The structure of phase Q223 (space group Pm3n). An X-ray scattering study. *J Mol Biol* 225(1):137–145.
8. Sakamoto Y, et al. (2000) Direct imaging of the pores and cages of three-dimensional mesoporous materials. *Nature* 408(6811):449–453.
9. Che S, et al. (2003) A novel anionic surfactant templating route for synthesizing mesoporous silica with unique structure. *Nat Mater* 2(12):801–805.
10. Lee S, Bluemle MJ, Bates FS (2010) Discovery of a Frank-Kasper sigma phase in sphere-forming block copolymer melts. *Science* 330(6002):349–353.
11. Lee S, Leighton C, Bates FS (2014) Sphericity and symmetry breaking in the formation of Frank-Kasper phases from one component materials. *Proc Natl Acad Sci USA* 111(50):17723–17731.
12. Hayashida K, Dotera T, Takano A, Matsushita Y (2007) Polymeric quasicrystal: Mesoscopic quasicrystalline tiling in ABC star polymers. *Phys Rev Lett* 98(19):195502.
13. Hudson SD, et al. (1997) Direct visualization of individual cylindrical and spherical supramolecular dendrimers. *Science* 278(5337):449–452.
14. Ungar G, Liu Y, Zeng X, Percec V, Cho WD (2003) Giant supramolecular liquid crystal lattice. *Science* 299(5610):1208–1211.
15. Rosen BM, et al. (2009) Dendron-mediated self-assembly, disassembly, and self-organization of complex systems. *Chem Rev* 109(11):6275–6540.
16. Cheng XH, Diele S, Tschierske C (2000) Molecular design of liquid-crystalline block molecules: Semifluorinated pentaerythritol tetrabenzoates exhibiting lamellar, columnar, and cubic mesophases. *Angew Chem Int Ed Engl* 39(3):592–595.
17. Ungar G, Zeng X (2005) Frank–Kasper, quasicrystalline and related phases in liquid crystals. *Soft Matter* 1(2):95–106.
18. Shevchenko EV, Talapin DV, Kotov NA, O'Brien S, Murray CB (2006) Structural diversity in binary nanoparticle superlattices. *Nature* 439(7072):55–59.
19. Huang M, et al. (2015) Selective assemblies of giant tetrahedra via precisely controlled positional interactions. *Science* 348(6233):424–428.
20. Xiao C, Fujita N, Miyasaka K, Sakamoto Y, Terasaki O (2012) Dodecagonal tiling in mesoporous silica. *Nature* 487(7407):349–353.
21. Fischer S, et al. (2011) Colloidal quasicrystals with 12-fold and 18-fold diffraction symmetry. *Proc Natl Acad Sci USA* 108(5):1810–1814.
22. Zeng X, et al. (2004) Supramolecular dendritic liquid quasicrystals. *Nature* 428(6979):157–160.
23. Zhang J, Bates FS (2012) Dodecagonal quasicrystalline morphology in a poly(styrene-b-isoprene-b-styrene-b-ethylene oxide) tetrablock terpolymer. *J Am Chem Soc* 134(18):7636–7639.
24. Gillard TM, Lee S, Bates FS (2016) Dodecagonal quasicrystalline order in a diblock copolymer melt. *Proc Natl Acad Sci USA* 113(19):5167–5172.
25. Chanpuriya S, et al. (2016) Cornucopia of nanoscale ordered phases in sphere-forming tetrablock terpolymers. *ACS Nano* 10(5):4961–4972, 10.1021/acsnano.1026b00495.
26. Grason GM, DiDonna BA, Kamien RD (2003) Geometric theory of diblock copolymer phases. *Phys Rev Lett* 91(5):058304.
27. Xie N, Li W, Qiu F, Shi A-C (2014) σ Phase formed in conformationally asymmetric AB-type block copolymers. *ACS Macro Lett* 3(9):906–910.
28. Zhang X, Chan ER, Glotzer SC (2005) Self-assembled morphologies of monotethered polyhedral oligomeric silsesquioxane nanocubes from computer simulation. *J Chem Phys* 123(18):184718.
29. Chan ER, Zhang X, Lee C-Y, Neurock M, Glotzer SC (2005) Simulations of tetra-tethered organic/inorganic nanocube-polymer assemblies. *Macromolecules* 38(14):6168–6180.
30. Yue K, et al. (2012) Sequential "click" approach to polyhedral oligomeric silsesquioxane-based shape amphiphiles. *Macromolecules* 45(20):8126–8134.
31. Yue K, et al. (2013) Exploring shape amphiphiles beyond giant surfactants: Molecular design and click synthesis. *Polym Chem* 4(4):1056–1067.
32. Yue K, et al. (2013) Anionic synthesis of a "clickable" middle-chain azidefunctionalized polystyrene and its application in shape amphiphiles. *Chin J Polym Sci* 31(1):71–82.
33. Yu X, et al. (2013) Giant surfactants provide a versatile platform for sub-10-nm nanostructure engineering. *Proc Natl Acad Sci USA* 110(25):10078–10083.
34. Iacovella CR, Keys AS, Glotzer SC (2011) Self-assembly of soft-matter quasicrystals and their approximants. *Proc Natl Acad Sci USA* 108(52):20935–20940.
35. Ziherl P, Kamien RD (2000) Soap froths and crystal structures. *Phys Rev Lett* 85(16):3528–3531.
36. Marson RL, Phillips CL, Anderson JA, Glotzer SC (2014) Phase behavior and complex crystal structures of self-assembled tethered nanoparticle telechelics. *Nano Lett* 14(4):2071–2078.